Article

A dusty veil shading Betelgeuse during its Great Dimming

https://doi.org/10.1038/s41586-021-03546-8

Received: 6 November 2020

Accepted: 13 April 2021

Published online: 16 June 2021

Check for updates

M. Montargès[1,2]✉, E. Cannon[2], E. Lagadec[3], A. de Koter[2,4], P. Kervella[1], J. Sanchez-Bermudez[5,6], C. Paladini[7], F. Cantalloube[5], L. Decin[2,8], P. Scicluna[7], K. Kravchenko[9], A. K. Dupree[10], S. Ridgway[11], M. Wittkowski[12], N. Anugu[13,14], R. Norris[15], G. Rau[16,17], G. Perrin[1], A. Chiavassa[3], S. Kraus[14], J. D. Monnier[18], F. Millour[3], J.-B. Le Bouquin[18,19], X. Haubois[7], B. Lopez[3], P. Stee[3] & W. Danchi[16]

Red supergiants are the most common final evolutionary stage of stars that have initial masses between 8 and 35 times that of the Sun[1]. During this stage, which lasts roughly 100,000 years[1], red supergiants experience substantial mass loss. However, the mechanism for this mass loss is unknown[2]. Mass loss may affect the evolutionary path, collapse and future supernova light curve[3] of a red supergiant, and its ultimate fate as either a neutron star or a black hole[4]. From November 2019 to March 2020, Betelgeuse—the second-closest red supergiant to Earth (roughly 220 parsecs, or 724 light years, away)[5,6]—experienced a historic dimming of its visible brightness. Usually having an apparent magnitude between 0.1 and 1.0, its visual brightness decreased to 1.614 ± 0.008 magnitudes around 7–13 February 2020[7]—an event referred to as Betelgeuse's Great Dimming. Here we report high-angular-resolution observations showing that the southern hemisphere of Betelgeuse was ten times darker than usual in the visible spectrum during its Great Dimming. Observations and modelling support a scenario in which a dust clump formed recently in the vicinity of the star, owing to a local temperature decrease in a cool patch that appeared on the photosphere. The directly imaged brightness variations of Betelgeuse evolved on a timescale of weeks. Our findings suggest that a component of mass loss from red supergiants[8] is inhomogeneous, linked to a very contrasted and rapidly changing photosphere.

We obtained direct high-spatial-resolution observations of Betelgeuse using the SPHERE instrument on the Very Large Telescope (VLT) and the GRAVITY instrument on the VLT Interferometer (VLTI). Details on these instruments and on data acquisition and reduction are available in Methods. The SPHERE images, obtained in the visual domain with the Zurich imaging polarimeter (ZIMPOL), provide the only resolved reconnaissance of the stellar disk and its nearby surroundings a year before and throughout the Great Dimming event. Observations were secured before (January 2019) and during the dimming (December 2019 and January and March 2020; Fig. 1).

The deconvolved ZIMPOL images of Betelgeuse for the four epochs are presented in Fig. 2. The photosphere of Betelgeuse is clearly resolved in each image, with deviations from circular symmetry. Imaging in March 2015[9] showed an elongation along the north–east to south–west axis. The same shape is apparent in our January 2019 image (Fig. 2a), but less pronounced. In December 2019 and January 2020 (Fig. 2b, c), in all filters, the southern hemisphere of the star has a peak brightness more than ten times less than the northern hemisphere.

Four scenarios could explain the Great Dimming of Betelgeuse: (1) a (potentially local) decrease in the effective temperature of the star, making it fainter; (2) an occultation by newly formed dust; (3) an occultation by dust transiting in front of the star; or (4) a change in the angular diameter. We check each scenario against our observations.

A transiting dusty clump (scenario 3) is rejected because such a clump should change quadrant before and after the deepest dimming, whereas our observations in January and March 2020 show that the dark area remained in the southwest quadrant. A change in diameter (scenario 4) is ruled out by our VLTI/GRAVITY and VLT/SPHERE–IRDIS (Infrared Dual-Beam Imager and Spectrograph) observations. We measured uniform-disk angular diameters of $\theta_{UD} = 42.61 \pm 0.05$ mas in January 2019 and $\theta_{UD} = 42.11 \pm 0.05$ mas (here and elsewhere, the errors quoted refer to $\pm 1\sigma$) in February 2020, well within the range explored during

[1]LESIA, Observatoire de Paris, Université PSL, CNRS, Sorbonne Université, Université de Paris, Meudon, France. [2]Institute of Astronomy, KU Leuven, Leuven, Belgium. [3]Université Côte d'Azur, Observatoire de la Côte d'Azur, CNRS, Laboratoire Lagrange, France. [4]Anton Pannenkoek Institute for Astronomy, University of Amsterdam, Amsterdam, The Netherlands. [5]Max Planck Institute for Astronomy, Heidelberg, Germany. [6]Instituto de Astronomía, Universidad Nacional Autónoma de México, Ciudad de México, Mexico. [7]European Southern Observatory, Santiago, Chile. [8]School of Chemistry, University of Leeds, Leeds, UK. [9]Max Planck Institute for Extraterrestrial Physics, Garching, Germany. [10]Center for Astrophysics | Harvard and Smithsonian, Cambridge, MA, USA. [11]NSF's National Optical-Infrared Astronomy Research Laboratory, Tucson, AZ, USA. [12]European Southern Observatory, Garching bei München, Germany. [13]Steward Observatory, University of Arizona, Tucson, AZ, USA. [14]School of Physics and Astronomy, University of Exeter, Exeter, UK. [15]Physics Department, New Mexico Institute of Mining and Technology, Socorro, NM, USA. [16]Exoplanets and Stellar Astrophysics Laboratory, NASA Goddard Space Flight Center, Greenbelt, MD, USA. [17]Department of Physics, Catholic University of America, Washington, DC, USA. [18]Department of Astronomy, University of Michigan, Ann Arbor, MI, USA. [19]IPAG, Université Grenoble Alpes, CNRS, Grenoble, France. ✉e-mail: miguel.montarges@observatoiredeparis.psl.eu

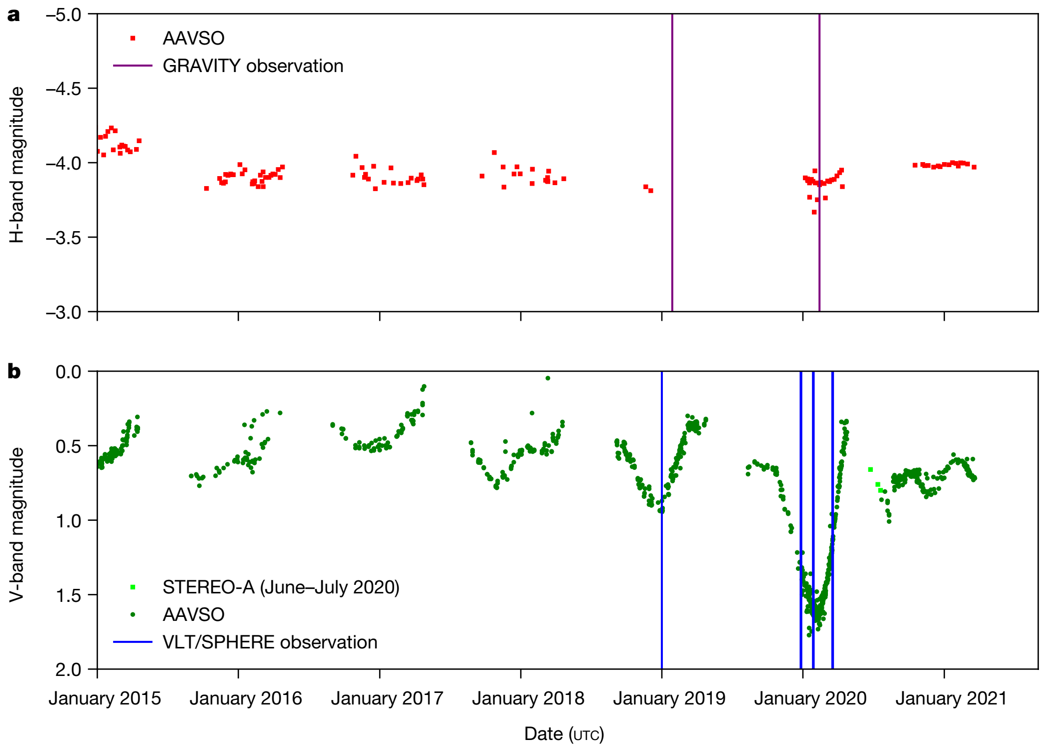

Fig. 1 | Light curve of Betelgeuse over the past six years. Data were obtained from the AAVSO and the space-based solar observatory STEREO-A[40]. The dates of the observations presented here are indicated by vertical lines. **a**, Near-infrared. **b**, Visible.

the past 30 years[10] and far from the 30% variation required to produce the visible dimming.

Dust has previously been inferred from spectrophotometric observations[11]. However, TiO photometry[12] and submillimetre observations[13] suggest that one or more dark and cool photospheric spots better explain the event while preserving compatibility with optical spectrophotometry; this explanation evidences an increase in molecular opacity. A similar conclusion is reached on the basis of tomography from high-resolution spectroscopy, which suggests that the propagation of two shock waves in the upper atmosphere, aided by underlying convection or outward gas motion, altered the molecular opacity of the star in the line of sight[14]. This scenario is compatible with anterior spectropolarimetric imaging[15] and three-dimensional simulations of stellar convection in evolved stars carried out using the CO5BOLD code[16–19]. Here, convection is expected to trigger the formation of gas clumps capable of causing dimming events. We explore both hypotheses: a photospheric cooling and the formation of dust (scenarios 1 and 2, respectively).

We explore the cool-patch hypothesis by building a composite PHOENIX model[20] of the stellar photosphere. The composite model images are then convolved with the ZIMPOL beam and compared to our observations. With the unperturbed photospheric temperature[11] set to 3,700 K, we determine the best-matching cool patch temperatures to be 3,400 K in December 2019 and January 2020 and 3,200 K in March 2020. The cool region has a best-matching extent of 62%, 79% and 43% of the apparent disk, respectively, for these three epochs. All temperatures are given with a 50 K uncertainty, which corresponds to the PHOENIX grid spacing.

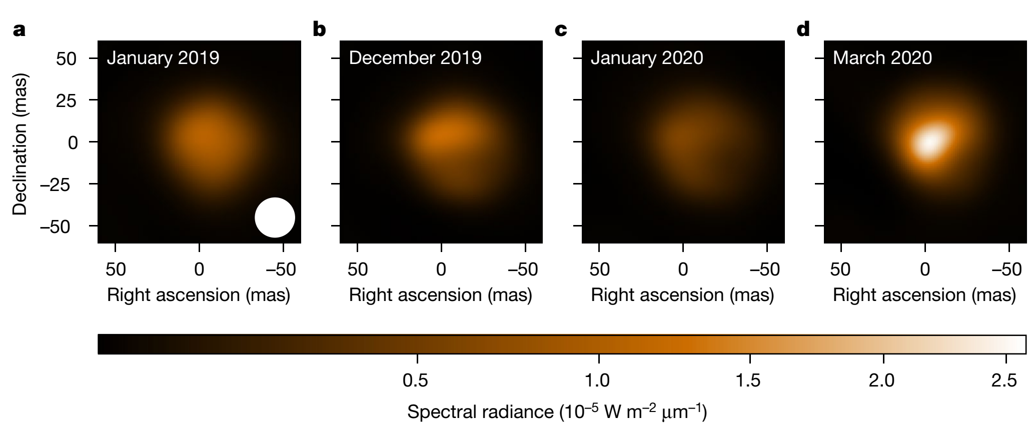

Fig. 2 | VLT/SPHERE–ZIMPOL observations of Betelgeuse after deconvolution in the Cnt_Hα filter. North is up; east is left. The beam size of ZIMPOL is indicated by the white disk in **a**. We used a power-law scale intensity with an index of 0.65 to enhance the contrast. **a**, January 2019. **b**, December 2019. **c**, January 2020. **d**, March 2020. The Cnt_Hα filter (one of ZIMPOL's filters) is centred at 644.9 nm (see Extended Data Table 1 for details).

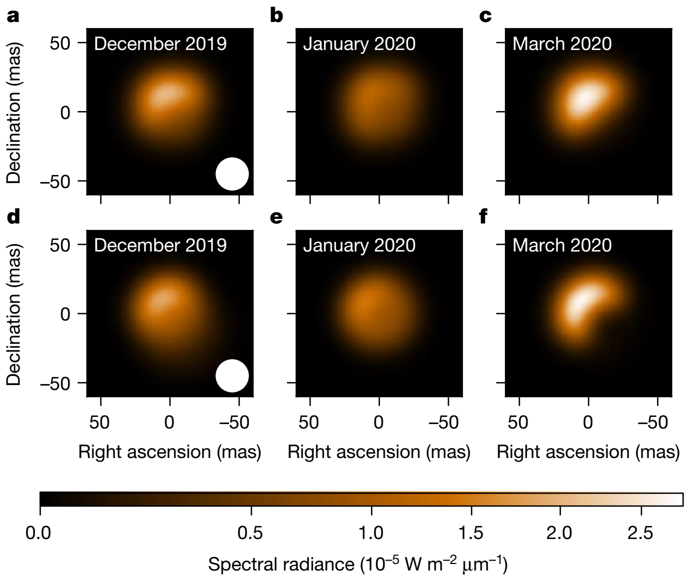

Fig. 3 | Best model images obtained in the Cnt_Hα filter. The images have been convolved with the SPHERE beam. **a**–**c**, Best-matching PHOENIX composite model (a cool spot). **d**–**f**, Best RADMC3D simulations (a dusty clump). We used a power-law scale intensity with an index of 0.65 to enhance the contrast. **a**, **d**, December 2019. **b**, **e**, January 2020. **c**, **f**, March 2020.

The dust-clump hypothesis is investigated using RADMC3D[21] dust radiative transfer simulations. By exploring a grid of input parameters for a spherical dusty clump of constant density illuminated and heated by the red supergiant, we derive optimized values for December 2019. For January and March 2020, the parameters were tuned manually to reproduce the peculiar shape of the images, which proved very sensitive to the inputs. We retrieve clump radii of 4.5–6 AU, or about the stellar radius, and total dust masses of $(3–13)\times10^{-10}M_{\odot}$ (where $M_{\odot}$ is the mass of the Sun). Assuming a gas-to-dust ratio in the environment of red supergiants[22] of roughly 200, we infer a total mass of the clump of $(0.7–3)\times10^{-7}M_{\odot}$ ($(2.3–8.5)\times10^{-2}$ Earth masses). This mass represents 35%–128% of the average annual mass loss from Betelgeuse assuming a low mass-loss rate ($2.1\times10^{-7}M_{\odot}\,yr^{-1}$)[23] or 3%–12% assuming a high mass-loss-rate ($(2\pm1)\times10^{-6}M_{\odot}\,yr^{-1}$)[24].

Images of both types of model for the three observed dimmed epochs are plotted in Fig. 3, showing qualitative morphological agreement with the observations. The cool-patch and dusty-clump models both capture the essential behaviour during the Great Dimming; that is, they both recover the level of optical dimming and the first-order atmospheric structure seen during the event. However, both models predict a decrease in J-band near-infrared brightness by a factor of 1.2–1.3, whereas a factor of only 1.02 is observed (Fig. 1, Extended Data Fig. 1). Variations in the chemical composition, shape and properties of solid species in the dust occultation model, or a temporary change in photospheric molecular opacities, probably reconcile the H-band flux and reproduces the American Association of Variable Star Observers (AAVSO) photometry in this spectral domain.

Some observations of the Great Dimming clearly identify the presence of newly formed dust close to the photosphere[25,26], whereas other studies identify a cooling of the photosphere[13]. The Great Dimming occurred 424 ± 4 days after the star's previous minimum[7]. Given a primary pulsation period of about 400 days[27], the scenario that explains the event must account for the alignment with the pulsation behaviour of the star. We propose that some time before the Great Dimming the star ejected a bubble of gas, probably at a favourable incidence in the pulsation cycle and potentially aided by the surfacing of a giant convective cell[28]. The critical parameter to allow for dust condensation in the ambient environment of cool evolved stars is the temperature[29]. The gas cloud may have been present in the near circumstellar environment, but it would have been too warm to trigger dust nucleation, until the star decreased in brightness in late 2019, in accordance with its pulsation phase. According to the RADMC3D modelling, with a local decrease in surface temperature from 3,700 K to 3,400 K in December 2019, the temperature of the environment surrounding the clump must have decreased from 2,300–1,900 K to 2,000–1,600 K at 12.5 AU, which may have initiated rapid dust formation[30]. After the initial dust nucleation and obscuration, the gas further out is screened from the star, which may have triggered a dust nucleation cascade that caused the Great Dimming. Although a fully consistent ab initio three-dimensional hydro-chemical model for such a scenario has not yet been developed for an M-type red supergiant[29], the explanation we outline resembles remarkably the scenario proposed for R Coronae Borealis stars, including the coincidence of the dimming with the pulsation minimum[31].

Our observations from December 2019 to March 2020 demonstrate in real time a discrete mass-loss event from a red supergiant. This mass loss is nonuniform and episodic, unambiguously linking the initiation mechanism to local surface behaviour—that is, a contrasted and rapidly changing photosphere. The released gas cloud experiences dust nucleation within a few stellar radii, which may have an essential role in letting the ejected material escape from the system.

If such dusty-cloud ejections are a recurrent phenomenon, which observations of other red supergiants suggest may be the case[32,33], then only a fraction of these events may happen in the line of sight towards Earth and lead to obscuration of stellar light. Betelgeuse's AAVSO light curve (Extended Data Fig. 2) shows another possible dimming in 1984–1986, when some visual magnitude measurements decreased to 2 mag. However, only two observers out of several tens saw it. Further, although these two visual observers saw Betelgeuse at a visual magnitude of 1.8–2, photoelectric measurements in the V band were at 0.7 mag. The 2019–2020 extreme dimming of Betelgeuse seems to be the only confirmed example for this star over the past century.

Previous observations of the circumstellar environment of Betelgeuse[8,34–37] show a very inhomogeneous environment embedded in a smoother matrix. This may confirm that Betelgeuse and possibly other red supergiants experience two modes of mass loss[8,38,39]: a smooth homogeneous radial outflow that consists mainly of gas, with partial dust nucleation potentially occurring farther from the star; and an episodic localized ejection of gas clumps where conditions are favourable for efficient dust formation while still close to the photosphere.

Photometric observations of the star continued after the Great Dimming. Measurements[40] obtained in June–July 2020 show that Betelgeuse experienced another dimming that did not correspond to the 400-day period, but it has since recovered[41]. These successive dimmings fall within the irregular pattern of light-curve variability of the star and may be attributed to pulsation or convective activity[6].

Our results confirm that the Great Dimming is not an indication of Betelgeuse's imminent explosion as a supernova[6,24]. The early behaviour of light curves for core-collapse supernova and the post-collapse spectral line variation point to enhanced pre-supernova mass loss in the final weeks to centuries of the stars' lives[42], in at least part of the progenitor population. For the longest timescale, these enhanced rates may amount to roughly $10^{-4}M_{\odot}\,yr^{-1}$; for the shorter timescales, they may be as high as around $1M_{\odot}\,yr^{-1}$ (ref. [43]). With a current mass-loss rate[23,24] between $2\times10^{-7}M_{\odot}\,yr^{-1}$ and $2\times10^{-6}M_{\odot}\,yr^{-1}$, Betelgeuse does not (yet) seem to have entered such a phase. Pre-supernova activity possibly related to instabilities in nuclear burning[44,45] or to waves driven by vigorous core convection[42,46] has been reported for several type IIP progenitors in the few years before explosion[47,48]. However, a minority of the type IIP/L progenitor population may show visual variability of no more than 5%–10% in these final years, with the possible exception of short outbursts on a timescale of months[49]. This means that some red supergiants may show little or no sign of their impending core collapse, years to weeks before it happens. Therefore, although the current mass-loss behaviour of Betelgeuse does not appear to forebode its demise, it remains possible that it may explode without warning.

Online content

Any methods, additional references, Nature Research reporting summaries, source data, extended data, supplementary information, acknowledgements, peer review information; details of author contributions and competing interests; and statements of data and code availability are available at https://doi.org/10.1038/s41586-021-03546-8.

1. Ekström, S. et al. Grids of stellar models with rotation. I. Models from 0.8 to 120 $M_\odot$ at solar metallicity (Z = 0.014). *Astron. Astrophys*. **537**, A146 (2012).
2. Arroyo-Torres, B. et al. What causes the large extensions of red supergiant atmospheres? Comparisons of interferometric observations with 1D hydrostatic, 3D convection, and 1D pulsating model atmospheres. *Astron. Astrophys*. **575**, A50 (2015).
3. Moriya, T. J., Förster, F., Yoon, S.-C., Gräfener, G. & Blinnikov, S. I. Type IIP supernova light curves affected by the acceleration of red supergiant winds. *Mon. Not. R. Astron. Soc*. **476**, 2840–2851 (2018).
4. Meynet, G. et al. Impact of mass-loss on the evolution and pre-supernova properties of red supergiants. *Astron. Astrophys*. **575**, A60 (2015).
5. Harper, G. M. et al. An updated 2017 astrometric solution for Betelgeuse. *Astron. J*. **154**, 11 (2017).
6. Joyce, M. et al. Standing on the shoulders of giants: new mass and distance estimates for Betelgeuse through combined evolutionary, asteroseismic, and hydrodynamic simulations with MESA. *Astrophys. J*. **902**, 63 (2020).
7. Guinan, E., Wasatonic, R., Calderwood, T. & Carona, D. The fall and rise in brightness of Betelgeuse. *Astron. Telegr*. 13512 (2020).
8. Kervella, P. et al. The close circumstellar environment of Betelgeuse. II. Diffraction-limited spectro-imaging from 7.76 to 19.50 μm with VLT/VISIR. *Astron. Astrophys*. **531**, A117 (2011).
9. Kervella, P. et al. The close circumstellar environment of Betelgeuse. III. SPHERE/ZIMPOL imaging polarimetry in the visible. *Astron. Astrophys*. **585**, A28 (2016).
10. Ohnaka, K. et al. Imaging the dynamical atmosphere of the red supergiant Betelgeuse in the CO first overtone lines with VLTI/AMBER. *Astron. Astrophys*. **529**, A163 (2011).
11. Levesque, E. M. & Massey, P. Betelgeuse just is not that cool: effective temperature alone cannot explain the recent dimming of Betelgeuse. *Astrophys. J*. **891**, L37 (2020).
12. Harper, G. M., Guinan, E. F., Wasatonic, R. & Ryde, N. The photospheric temperatures of Betelgeuse during the Great Dimming of 2019/2020: no new dust required. *Astrophys. J*. **905**, 34 (2020).
13. Dharmawardena, T. E. et al. Betelgeuse fainter in the submillimeter too: an analysis of JCMT and APEX monitoring during the recent optical minimum. *Astrophys. J*. **897**, L9 (2020).
14. Kravchenko, K. et al. Atmosphere of Betelgeuse before and during the great dimming revealed by tomography. *Astron. Astrophys*. https://doi.org/10.1051/0004-6361/202039801 (in the press).
15. López Ariste, A. et al. Convective cells in Betelgeuse: imaging through spectropolarimetry. *Astron. Astrophys*. **620**, A199 (2018).
16. Freytag, B., Steffen, M. & Dorch, B. Spots on the surface of Betelgeuse – results from new 3D stellar convection models. *Astron. Nachr*. **323**, 213–219 (2002).
17. Freytag, B. et al. Simulations of stellar convection with CO5BOLD. *J. Comput. Phys*. **231**, 919–959 (2012).
18. Chiavassa, A., Freytag, B., Masseron, T. & Plez, B. Radiative hydrodynamics simulations of red supergiant stars. IV. Gray versus non-gray opacities. *Astron. Astrophys*. **535**, A22 (2011).
19. Freytag, B., Liljegren, S. & Höfner, S. Global 3D radiation-hydrodynamics models of AGB stars. Effects of convection and radial pulsations on atmospheric structures. *Astron. Astrophys*. **600**, A137 (2017).
20. Lançon, A., Hauschildt, P. H., Ladjal, D. & Mouhcine, M. Near-IR spectra of red supergiants and giants. I. Models with solar and with mixing-induced surface abundance ratios. *Astron. Astrophys*. **468**, 205–220 (2007).
21. Dullemond, C. P. et al. RADMC-3D: a multi-purpose radiative transfer tool. *Astrophysics Source Code Library* http://ascl.net/1202.015 (2012).
22. Mauron, N. & Josselin, E. The mass-loss rates of red supergiants and the de Jager prescription. *Astron. Astrophys*. **526**, A156 (2011).
23. De Beck, E. et al. Probing the mass-loss history of AGB and red supergiant stars from CO rotational line profiles. II. CO line survey of evolved stars: derivation of mass-loss rate formulae. *Astron. Astrophys*. **523**, A18 (2010).
24. Dolan, M. M. et al. Evolutionary tracks for Betelgeuse. *Astrophys. J*. **819**, 7 (2016).
25. Cotton, D. V., Bailey, J., Horta, A. D., Norris, B. R. M. & Lomax, J. R. Multi-band aperture polarimetry of Betelgeuse during the 2019–20 dimming. *Res. Notes Am. Astron. Soc*. **4**, 39 (2020); erratum **4**, 47 (2020).
26. Safonov, B. et al. Differential speckle polarimetry of Betelgeuse in 2019–2020: the rise is different from the fall. Preprint at https://arXiv.org/abs/2005.05215 (2020).
27. Stothers, R. B. Giant convection cell turnover as an explanation of the long secondary periods in semiregular red variable stars. *Astrophys. J*. **725**, 1170–1174 (2010).
28. Dupree, A. K. et al. Spatially resolved ultraviolet spectroscopy of the Great Dimming of Betelgeuse. *Astrophys. J*. **899**, 68 (2020).
29. Höfner, S. & Freytag, B. Exploring the origin of clumpy dust clouds around cool giants. A global 3D RHD model of a dust-forming M-type AGB star. *Astron. Astrophys*. **623**, A158 (2019).
30. Boulangier, J., Gobrecht, D., Decin, L., de Koter, A. & Yates, J. Developing a self-consistent AGB wind model – II. Non-classical, non-equilibrium polymer nucleation in a chemical mixture. *Mon. Not. R. Astron. Soc*. **489**, 4890–4911 (2019).
31. Fadeyev, I. A. Carbon dust formation in R Coronae Borealis stars. *Mon. Not. R. Astron. Soc*. **233**, 65–78 (1988).
32. Ohnaka, K. Imaging the outward motions of clumpy dust clouds around the red supergiant Antares with VLT/VISIR. *Astron. Astrophys*. **568**, A17 (2014).
33. Scicluna, P. et al. Large dust grains in the wind of VY Canis Majoris. *Astron. Astrophys*. **584**, L10 (2015).
34. Kervella, P. et al. The close circumstellar environment of Betelgeuse. Adaptive optics spectro-imaging in the near-IR with VLT/NACO. *Astron. Astrophys*. **504**, 115–125 (2009).
35. O'Gorman, E. et al. CARMA CO(J = 2 − 1) Observations of the Circumstellar Envelope of Betelgeuse. *Astron. J*. **144**, 36 (2012).
36. Decin, L. et al. The enigmatic nature of the circumstellar envelope and bow shock surrounding Betelgeuse as revealed by Herschel. I. Evidence of clumps, multiple arcs, and a linear bar-like structure. *Astron. Astrophys*. **548**, A113 (2012).
37. Kervella, P. et al. The close circumstellar environment of Betelgeuse. V. Rotation velocity and molecular envelope properties from ALMA. *Astron. Astrophys*. **609**, A67 (2018).
38. Humphreys, R. M., Helton, L. A. & Jones, T. J. The three-dimensional morphology of VY Canis Majoris. I. The kinematics of the ejecta. *Astron. J*. **133**, 2716–2729 (2007).
39. Smith, N., Hinkle, K. H. & Ryde, N. Red supergiants as potential type IIn supernova progenitors: spatially resolved 4.6 μm CO emission around VY CMa and Betelgeuse. *Astron. J*. **137**, 3558–3573 (2009).
40. Dupree, A., Guinan, E., Thompson, W. T. & STEREO/SECCHI/HI Consortium. Photometry of Betelgeuse with the STEREO mission while in the glare of the Sun from Earth. *Astron. Telegr*. 13901 (2020).
41. Sigismondi, C. et al. Second dust cloud on Betelgeuse. *Astron. Telegr*. 13982 (2020).
42. Fuller, J. Pre-supernova outbursts via wave heating in massive stars – I. Red supergiants. *Mon. Not. R. Astron. Soc*. **470**, 1642–1656 (2017).
43. Smith, N. et al. Endurance of SN 2005ip after a decade: X-rays, radio and Hα like SN 1988Z require long-lived pre-supernova mass-loss. *Mon. Not. R. Astron. Soc*. **466**, 3021–3034 (2017).
44. Smith, N. & Arnett, W. D. Preparing for an explosion: hydrodynamic instabilities and turbulence in presupernovae. *Astrophys. J*. **785**, 82 (2014).
45. Woosley, S. E. & Heger, A. The remarkable deaths of 9–11 solar mass stars. *Astrophys. J*. **810**, 34 (2015).
46. Quataert, E. & Shiode, J. Wave-driven mass loss in the last year of stellar evolution: setting the stage for the most luminous core-collapse supernovae. *Mon. Not. R. Astron. Soc*. **423**, L92–L96 (2012).
47. Yaron, O. et al. Confined dense circumstellar material surrounding a regular type II supernova. *Nat. Phys*. **13**, 510–517 (2017).
48. Andrews, J. E. et al. SN 2007od: a type IIP supernova with circumstellar interaction. *Astrophys. J*. **715**, 541–549 (2010).
49. Johnson, S. A., Kochanek, C. S. & Adams, S. M. The quiescent progenitors of four type II-P/L supernovae. *Mon. Not. R. Astron. Soc*. **480**, 1696–1704 (2018).

Methods

VLT/SPHERE–ZIMPOL observations

The resolved images were obtained using the spectropolarimetric high-contrast exoplanet research (SPHERE[50]) instrument, mounted on the third unit telescope of the European Southern Observatory's (ESO's) Very Large Telescope (VLT). More precisely, we used one of its sub-systems, the Zurich imaging polarimeter (ZIMPOL[51]). We observed Betelgeuse and a point-spread-function calibrator, Rigel, in the polarimetric P2 mode of ZIMPOL on 31 December 2018, 26 December 2019, 27 January 2020, and 18 and 20 March 2020. With an angular diameter of 2.76 ± 0.01 mas, Rigel[52] is well below the resolving power of ZIMPOL (24 mas). Both stars were observed with several filters. The log of the observations is presented in Extended Data Table 1. We used the publicly available ESOreflex/SPHERE pipeline (v0.38.0) to reduce the data and custom Python routines[53] to produce the observables. This enabled us to derive the total intensity, polarized flux, degree of linear polarization and polarization electric-vector position angle. The plate scale was 3.628 ± 0.036 mas per pixel. The average beam size of the ZIMPOL observations was 24 mas, or 1.14 times Betelgeuse's radius. We performed a flux calibration of the ZIMPOL data using Rigel as a flux reference. However, the result showed discrepancies between the different filters and with the AAVSO measurements for the V filter (Extended Data Fig. 1). We suspect that this issue results from the uncertainty on the transmission of the neutral densities used for the observations. Images at each epoch were deconvolved using the PyRAF-implemented Richardson–Lucy deconvolution algorithm, with Rigel as a measurement of the point spread function. To avoid producing deconvolution artefacts, only ten iterations were used on each frame. The result is visible in Fig. 2 and Extended Data Fig. 3.

VLT/SPHERE–IRDIS observations

We used the sparse aperture masking (SAM) mode[54] available on the infrared dual-band imager and spectrograph (IRDIS[55]), another subsystem of SPHERE, to complement the GRAVITY observations. The SAM mode uses a pupil mask with holes placed in a nonredundant configuration, designed to turn the single 8.2-m dish telescope into an array of seven 1.2-m-diameter circular subapertures. The goal was to obtain interferometric measurements well within the first lobe of the visibility function. Observations were taken in pupil-tracking mode, with the SPHERE seven-hole masks, using two filters: NB_CO (centre wavelength $\lambda_c = 2{,}290$; full-width at half-maximum FWHM = 33 nm) and NB_CntK2 (2,266 nm, FWHM = 32 nm). The log of the observations is presented in Extended Data Table 1. The data were reduced through the SPHERE data centre[56], applying the appropriate calibrations, following the data reduction and handling pipeline[57] to correct for bad pixels, dark current, flat field and sky background. Each frame was normalized in flux and the corresponding parallactic angle calculated. We then centred each image at the central lobe of the interferogram (using a two-dimensional Gaussian fit), cropped the images around this centre, and manually sorted out the images of the cube to remove frames with notable smearing or other sources of error such as residual bad pixels.

From the temporal cube of interferograms, the observables were extracted using a dedicated aperture masking data reduction software. The interferometric fringes created by each baseline of the nonredundant mask were fitted directly on the image plane[58,59]. Our pipeline does the model fitting of the fringes using single value decomposition, only the core of the interferogram is fitted and the software includes a bandwidth smearing correction. From the amplitude and phase of the fringes, squared visibilities and closure phases were obtained. Each frame in the data cubes was analysed independently. Subsequently, the mean and standard deviation (s.d.) of the observables per data cube were computed. The mean observables were calibrated using the aperture masking observations of the point-like reference stars reported in Extended Data Table 1. Finally, the different datasets per wavelength were averaged into an OIFITS file for analysis.

VLTI/GRAVITY observations

Betelgeuse and its interferometric calibrators were observed with GRAVITY[60] using the compact configuration (stations A0-B2-D0-C1) of the auxiliary telescopes of the VLT Interferometer (VLTI). We used the high-spectral-resolution ($\lambda/\Delta\lambda = 4{,}000$) and dual-polarization mode to accommodate for the brightness of Betelgeuse in the K band. The angular resolution reached was 14 mas. The log of the observations is presented in Extended Data Table 2. The data were reduced and calibrated through the ESOreflex pipeline (v1.2.4). We adopted angular diameters of 2.242 ± 0.212 mas for 56 Ori and 3.364 ± 0.283 mas for HD 44945 from the JMMC catalogue[61]. After the initial calibration, the two polarizations were averaged.

Angular diameter determination

The VLTI/GRAVITY and VLT/SPHERE–IRDIS SAM observations give us the squared visibility and closure phase as functions of the spatial frequency (B/λ, with B the baseline length and λ the wavelength). To estimate the angular diameter of the star, we built two datasets. The first contains the data before the dimming (IRDIS, 2019 January 01; GRAVITY, 2019 January 29); the second contains the data during the Great Dimming (IRDIS, 2019 December 27; GRAVITY, 2020 February 14). Because we do not expect the angular size of the star to change much on a scale of weeks, the time difference between the IRDIS and GRAVITY data for each set is negligible. We selected continuum data (CntK2 filter of the IRDIS observations and 2.22–2.28 μm for the GRAVITY data), thus excluding CO and water-vapour absorption bands. In addition, we excluded some weak atomic and molecular absorption lines in the K-band pseudo-continuum[62]. The angular diameter determination was done by fitting a uniform-disk model to the squared visibility data only. This model seems initially justified by the limited deviation from a centrosymmetric model in the closure phase (Extended Data Fig. 4) at low spatial frequency (for a centrosymmetric model, the closure phase should remain at 0° or 180°). To avoid contamination by small-scale structures, we limited the fit to the first lobe of visibility only (spatial frequency less than 6×10^6 rad^{-1}). We estimated the angular diameter of Betelgeuse to be $\theta_{UD} = 42.61 \pm 0.05$ mas (reduced $\chi^2 = 26.5$) before its dimming (January 2019) and $\theta_{UD} = 42.11 \pm 0.05$ mas (reduced $\chi^2 = 46.3$) during the dimming (December 2019 and February 2020). Fitting a limb-darkened disk does not provide any further improvement and does not substantially change the angular diameter. Therefore, because we are interested in only the variation in angular diameter between the two epochs, we retain the uniform-disk fit reasonable for the first lobe of the data in the continuum.

Pre-existing dust extinction

From previous studies[8,63], it is known that the circumstellar environment of Betelgeuse contains dust in an envelope around the star. However, this does not imply that the dust is present in a homogeneous way. Before looking at the extinction caused by the Great Dimming, we need to assess the amount of dust that was already in the line of sight, whether from circumstellar or interstellar origin. Therefore, we took into account the AAVSO V-, J- and H-band magnitude measurements obtained before the dimming started, simultaneously with our January 2019 SPHERE observations. The AAVSO error bars were re-estimated from 0.01 mag mostly to 0.1 mag to take into account the uncertainty on the magnitudes of the calibrator star. A possibility to model the already present circumstellar dust extinction is to include a spherical envelope around the star in a radiative transfer simulation. However, to limit the number of parameters, we instead fitted the extinction in the V band (A_V) required for the Cardelli[64] extinction law applied to the pre-dimming photometry to reproduce the PHOENIX[20] spectral energy distribution of a 15$M_\odot$ red supergiant. We adopted an effective temperature of T_{eff} = 3,600 K (following spectrophotometric measurements[11]) and surface gravity of log(g) = 0.0 (according to the literature[65], log(g) for Betelgeuse ranges from −0.32 to 0.43, with error bars up to 0.3). Because the ZIMPOL observations are performed through relatively broadband filters, we do not expect log(g) to be a sensitive parameter. Therefore, the dominant parameter in the selected spectral energy distribution is T_{eff}, which is well constrained from the spectrophotometry. We adopted R_V = 4.2 following red supergiant prescriptions[66] (with $R_V = A_V/E_{B-V}$ and E_{B-V} the colour excess $A_B - A_V$). The result gives A_V = 0.65.

Local-photospheric-cooling hypothesis

Considering the ZIMPOL images, if a dark, cool spot is the origin of the Great Dimming, we cannot use a simple photospheric model to reproduce it because surfaces with different T_{eff} must coexist. To reproduce our observations, we built a composite PHOENIX model: we filled a stellar disk with a warm (normal photosphere) and a cool (anomalous patch) PHOENIX photosphere[20]. The cool patch was circular, with four parameters: its temperature, its radius and the coordinates (x, y) of its centre. It is not allowed to expand outside the stellar disk. For each of the three epochs of the Great Dimming, we explored a grid of positions in the southwest quadrant in steps of 0.5 mas. We used the same step size for the radius in the range 0–10 mas. We explored the temperature pairs (3,200, 3,700) K, (3,300, 3,700) K and (3,400, 3,700) K for December 2019 and January 2020. For March 2020, we used the couples (3,200, 3700) K and (3,300, 3,800) K, owing to the higher contrast between the bright and dark areas. Note that here the warm photosphere was set at 3,700 K instead of the 3,600 K measured from spectrophotometric measurements[11], because we estimated that the latter value represents an average on patches with various temperatures. For each point of the grid, we computed the log-likelihood (L) of the model image with respect to the ZIMPOL observations. The goal was not to obtain a precise estimate of T_{eff}, but to assess the compatibility of this model with our images. Extended Data Fig. 5 shows the best images at each wavelength for each epoch. The best-matching parameters are summarized in Extended Data Table 3. The corresponding spectral energy distributions are plotted in Extended Data Fig. 1, along with the AAVSO and ZIMPOL photometry.

Dust-clump hypothesis

To test whether the ZIMPOL images and AAVSO photometry can be reproduced by the presence of a dust clump in the line of sight to Betelgeuse, we used a simulation based on the radiative transfer code RADMC3D[21]. The general scheme (coordinate system and physical parameters) of the simulation is illustrated in Extended Data Fig. 6. We used a spherical grid of 20^3 points, sampling radii from 5 AU to 50 AU, longitudinal angles from 0 to π and azimuthal angles from 0 to 2π. We used five levels of adaptive mesh refinement to resolve the clump. For clarity, all the coordinates below are given in the coordinate system described in Extended Data Fig. 6. The star was modelled as a PHOENIX photosphere[20] for a $15M_{\odot}$ red supergiant with T_{eff} = 3,700 K (3,800 K for March 2020) and log(g) = 0.0, according to parameters derived from spectrophotometric measurements[11]. We adopted a stellar size corresponding to the angular diameter measured with the VLT/SPHERE-IRDIS SAM and VLT/GRAVITY observations in December 2019 and January 2020, taking into account the distance[5] to the star. The dust clump was modelled as a spherical dust density centred at (x_c, y_c, z_c), with radius r_c, and constant dust density ρ_0. To converge on the best-fitting parameters, we ran a grid of RADMC3D models exploring a range of parameters for x_c and y_c (0 AU to −3 AU offset, with five steps), z_c (5 AU to 20 AU offset, with five steps), r_c (4 AU to 8 AU offset, with five steps) and ρ_0 (10^{-19} g cm^{-3} to 10^{-17} g cm^{-3}, with five steps logarithmically spaced). We adopted a canonical silicate composition for the dust ($MgFeSiO_4$)[67,68]. The sublimation temperature of this species is about 1,500 K, implying that for solutions that place the centre of the clump at about 11 AU part of the spherical clump volume closest to the star is devoid of this species. However, in at least the outer half of the dusty sphere, silicates may exist already at a clump centre distance of 11 AU. This differentiation of the chemical composition inside the clump does not affect our results (other than the actual dust distribution inside the dusty clump). The grain size distribution is centred at 0.21 μm (0.18–0.24 μm), chosen to have the maximum dimming effect in the visible range (among distributions centred at 0.1 μm, 0.21 μm, 0.5 μm and 1 μm, using comparisons with spectra and images). The dust opacity parameters were computed using RADMC3D's dedicated Python module based on Mie theory. The shape of the dust particles is assumed to be spherical (because we are not interested in reproducing the polarized signal), and the Gaussian grain size distribution was smeared out by 5% to avoid resonant effects. We refined these 3,125 models after a first iteration by adding two points to each parameter, around the initial optimization. This led to a total of 6,250 models. The best-matching model was found by computing the log-likelihood for each point of the grid with respect to the ZIMPOL images. For January and March 2020, such a grid was inefficient at finding a good enough combination of the parameters. The January 2020 and March 2020 models are not optimized, only best guesses. The best-matching parameters are summarized in Extended Data Table 3, the corresponding images in each ZIMPOL filter are shown in Extended Data Fig. 7 and the best-matching spectral energy distribution is plotted in Extended Data Fig. 1.

Data availability

Raw data were generated at the ESO under programs 0102.D-0240(A), 0102.D-0240(D), 104.20UZ and 104.20V6.004. Derived data that support the findings of this study are available at the Centre de Données Astronomiques de Strasbourg (CDS) via anonymous ftp to cdsarc.u-strasbg.fr (130.79.128.5) or via http://cdsarc.u-strasbg.fr/viz-bin/qcat?J/other/Nat (for the VLT/SPHERE–ZIMPOL images) and at the Optical Interferometry Database (OiDB; for the VLTI/GRAVITY and VLT/SPHERE–IRDIS SAM observations). Source data are provided with this paper.

Code availability

The SPHERE and GRAVITY pipelines are available on the ESO website (http://www.eso.org/sci/software/pipelines/index.html). The PyRAF implementation of the Richardson–Lucy deconvolution algorithm is publicly available at https://astroconda.readthedocs.io/en/latest/. The RADMC3D code is publicly available at https://github.com/dullemond/radmc3d-2.0.

50. Beuzit, J. L. et al. SPHERE: the exoplanet imager for the Very Large Telescope. *Astron. Astrophys.* **631**, A155 (2019).
51. Roelfsema, R. et al. The ZIMPOL high contrast imaging polarimeter for SPHERE: system test results. *Proc. SPIE* **9147**, 91473W (2014).
52. Chesneau, O. et al. Time, spatial, and spectral resolution of the Hα line-formation region of Deneb and Rigel with the VEGA/CHARA interferometer. *Astron. Astrophys.* **521**, A5 (2010).
53. Kervella, P. et al. The dust disk and companion of the nearby AGB star L_2 Puppis. SPHERE/ZIMPOL polarimetric imaging at visible wavelengths. *Astron. Astrophys.* **578**, A77 (2015).
54. Cheetham, A. C. et al. Sparse aperture masking with SPHERE. *Proc. SPIE* **9907**, 99072T (2016).
55. Dohlen, K. et al. The infra-red dual imaging and spectrograph for SPHERE: design and performance. *Proc. SPIE* **7014**, 70143L (2008).
56. Delorme, P. et al. The SPHERE data center: a reference for high contrast imaging processing. In *Proc. Annual Meeting of the French Society of Astronomy and Astrophysics* (eds Reylé, C. et al.) 347–361 (2017).
57. Pavlov, A. et al. SPHERE data reduction and handling system: overview, project status, and development. *Proc. SPIE* **7019**, 701939 (2008).
58. Lacour, S. et al. Sparse aperture masking at the VLT. I. Faint companion detection limits for the two debris disk stars HD 92945 and HD 141569. *Astron. Astrophys.* **532**, A72 (2011).
59. Greenbaum, A. Z., Pueyo, L., Sivaramakrishnan, A. & Lacour, S. An image-plane algorithm for JWST's non-redundant aperture mask data. *Astrophys. J.* **798**, 68 (2015).
60. Gravity Collaboration. First light for GRAVITY: phase referencing optical interferometry for the Very Large Telescope Interferometer. *Astron. Astrophys.* **602**, A94 (2017).
61. Duvert, G. JMDC: JMMC measured stellar diameters catalogue. *VizieR Online Data Catalog* II/345 (2016).

62. Ohnaka, K., Hadjara, M. & Maluenda Berna, M. Y. L. Spatially resolving the atmosphere of the non-Mira-type AGB star SW Vir in near-infrared molecular and atomic lines with VLTI/AMBER. *Astron. Astrophys*. **621**, A6 (2019).
63. Verhoelst, T. et al. The dust condensation sequence in red supergiant stars. *Astron. Astrophys*. **498**, 127–138 (2009).
64. Cardelli, J. A., Clayton, G. C. & Mathis, J. S. The relationship between infrared, optical, and ultraviolet extinction. *Astrophys. J*. **345**, 245–256 (1989).
65. Arentsen, A. et al. Stellar atmospheric parameters for 754 spectra from the X-shooter spectral library. *Astron. Astrophys*. **627**, A138 (2019).
66. Massey, P. et al. The reddening of red supergiants: when smoke gets in your eyes. *Astrophys. J*. **634**, 1286–1292 (2005).
67. Jaeger, C., Mutschke, H., Begemann, B., Dorschner, J. & Henning, T. Steps toward interstellar silicate mineralogy. 1: Laboratory results of a silicate glass of mean cosmic composition. *Astron. Astrophys*. **292**, 641–655 (1994).
68. Dorschner, J., Begemann, B., Henning, T., Jaeger, C. & Mutschke, H. Steps toward interstellar silicate mineralogy. II. Study of Mg-Fe-silicate glasses of variable composition. *Astron. Astrophys*. **300**, 503 (1995).
69. Tange, O. *GNU Parallel 2018* (Ole Tange, 2018).
70. Pérez, F. & Granger, B. E. IPython: a system for interactive scientific computing. *Comput. Sci. Eng*. **9**, 21–29 (2007).
71. van der Walt, S., Colbert, S. C. & Varoquaux, G. The NumPy array: a structure for efficient numerical computation. *Comput. Sci. Eng*. **13**, 22–30 (2011).
72. Hunter, J. D. Matplotlib: a 2D graphics environment. *Comput. Sci. Eng*. **9**, 90–95 (2007).
73. Virtanen, P. et al. SciPy 1.0: fundamental algorithms for scientific computing in Python. *Nat. Methods* **17**, 261–272 (2020); author correction **17**, 352 (2020).
74. McKinney, W. Data structures for statistical computing in Python. In *Proc. 9th Python in Science Conference* (eds van der Walt, S. & Millman. J) 56–61 (2010).
75. The Astropy Collaboration. Astropy: a community Python package for astronomy. *Astron. Astrophys*. **558**, A33 (2013).

Acknowledgements This research used variable star observations from the AAVSO International Database contributed by observers worldwide. This project received funding from the European Union's Horizon 2020 research and innovation programme under Marie Skłodowska-Curie grant agreement number 665501 with the research Foundation Flanders (FWO; [PEGASUS][2] Marie Curie fellowship 12U2717N awarded to M.M.). E.C. acknowledges funding from KU Leuven C1 grant MAESTRO C16/17/007. L.D. and M.M. acknowledge support from ERC consolidator grant 646758 AEROSOL. J.S.B. acknowledges the support received from the UNAM PAPIIT project IA 101220. S.K. acknowledges support from ERC starting grant 639889 ImagePlanetFormDiscs. The material is based on work supported by NASA under award number 80GSFC17M0002. We thank the ESO staff for their fast response in accepting the DDT proposal and carrying out the observations. We are grateful that Betelgeuse underwent this peculiar event more than 700 years ago in the appropriate solid angle. This work made use of the SPHERE data center, jointly operated by OSUG/IPAG (Grenoble), PYTHEAS/LAM/CeSAM (Marseille), OCA/Lagrange (Nice) and Observatoire de Paris/LESIA (Paris). This research made use of the Jean-Marie Mariotti Center Aspro and SearchCal services (http://www.jmmc.fr). We used the SIMBAD and VIZIER databases at CDS, Strasbourg (France; http://cdsweb.u-strasbg.fr/), and NASA's Astrophysics Data System Bibliographic Services. This research made use of GNU Parallel[69], IPython[70], Numpy[71], Matplotlib[72], SciPy[73], Pandas[74] (https://github.com/pandas-dev/pandas), Astropy[75] (http://www.astropy.org/) and Uncertainties (http://pythonhosted.org/uncertainties/).

Author contributions M.M. wrote the observing proposals, prepared all the observations, reduced and calibrated the ZIMPOL and GRAVITY data, ran the PHOENIX and RADMC3D simulations, made all the figures and is the main contributor to the text. E.C. cross-checked the RADMC3D modelling. E.L., J.S.-B. and F.C. reduced the SPHERE–IRDIS data. A.d.K. and L.D. wrote the discussion and conclusion. All authors contributed substantially to discussion, writing and revisions of the article.

Competing interests The authors declare no competing interests.

Additional information

Supplementary information The online version contains supplementary material available at https://doi.org/10.1038/s41586-021-03546-8.

Correspondence and requests for materials should be addressed to M.M.

Peer review information *Nature* thanks Manfred Cuntz, Edward Guinan and the other, anonymous, reviewer(s) for their contribution to the peer review of this work. Peer reviewer reports are available.

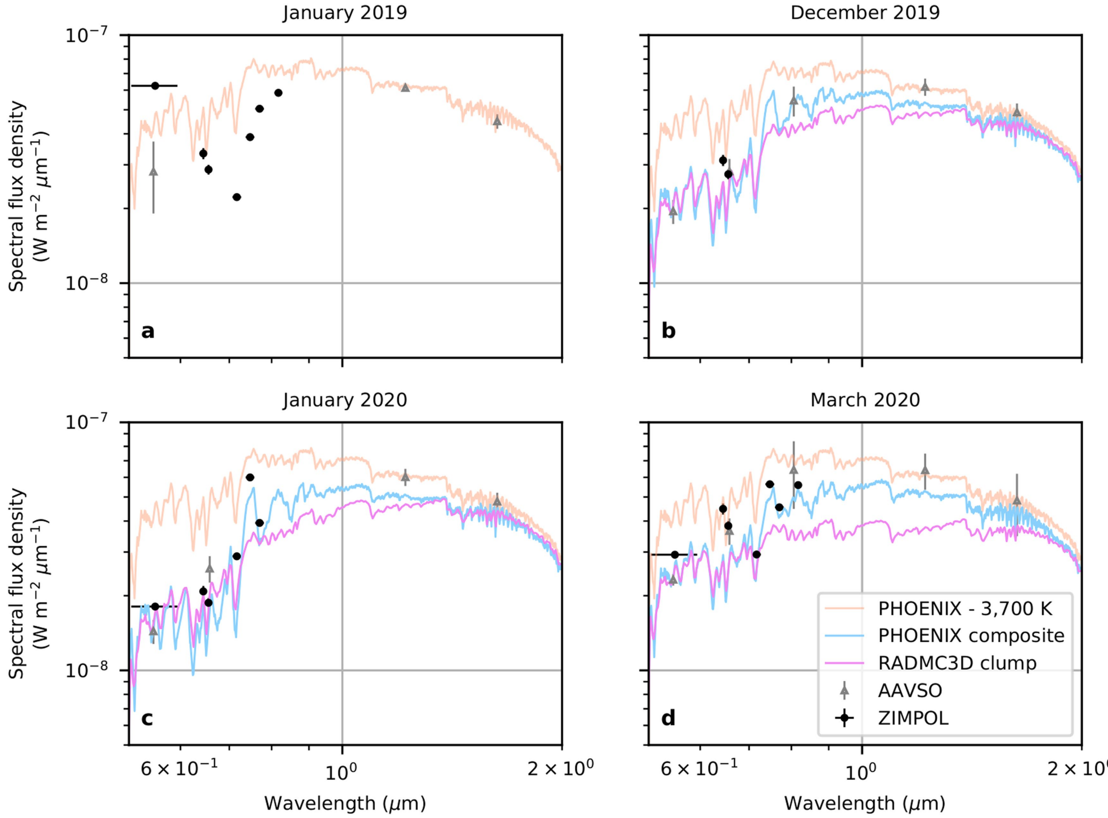

Extended Data Fig. 1 | Spectral energy distributions for the various epochs. **a**–**d**, Photometry from the ZIMPOL filters (black circles) and from the AAVSO measurements (grey triangles) is compared to a 3,700-K PHOENIX model (light orange), the best-matching composite PHOENIX model with a cool spot (blue) and best-matching RADMC3D dust clump model (violet). The flux error bars correspond to 1 s.d. The wavelength error bars correspond to the width of the ZIMPOL filters. The AAVSO error bars have been re-estimated from 0.01 mag mostly to 0.1 mag to take into account the uncertainty on the magnitudes of the calibrator star.

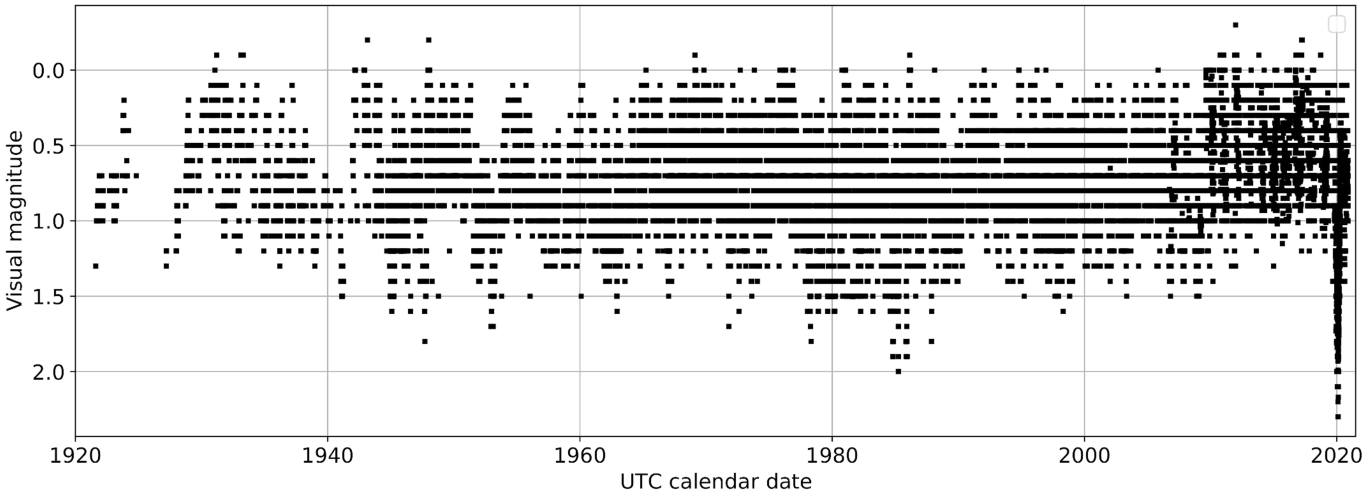

Extended Data Fig. 2 | Visual light curve of Betelgeuse. The data are taken from the AAVSO database over the past century.

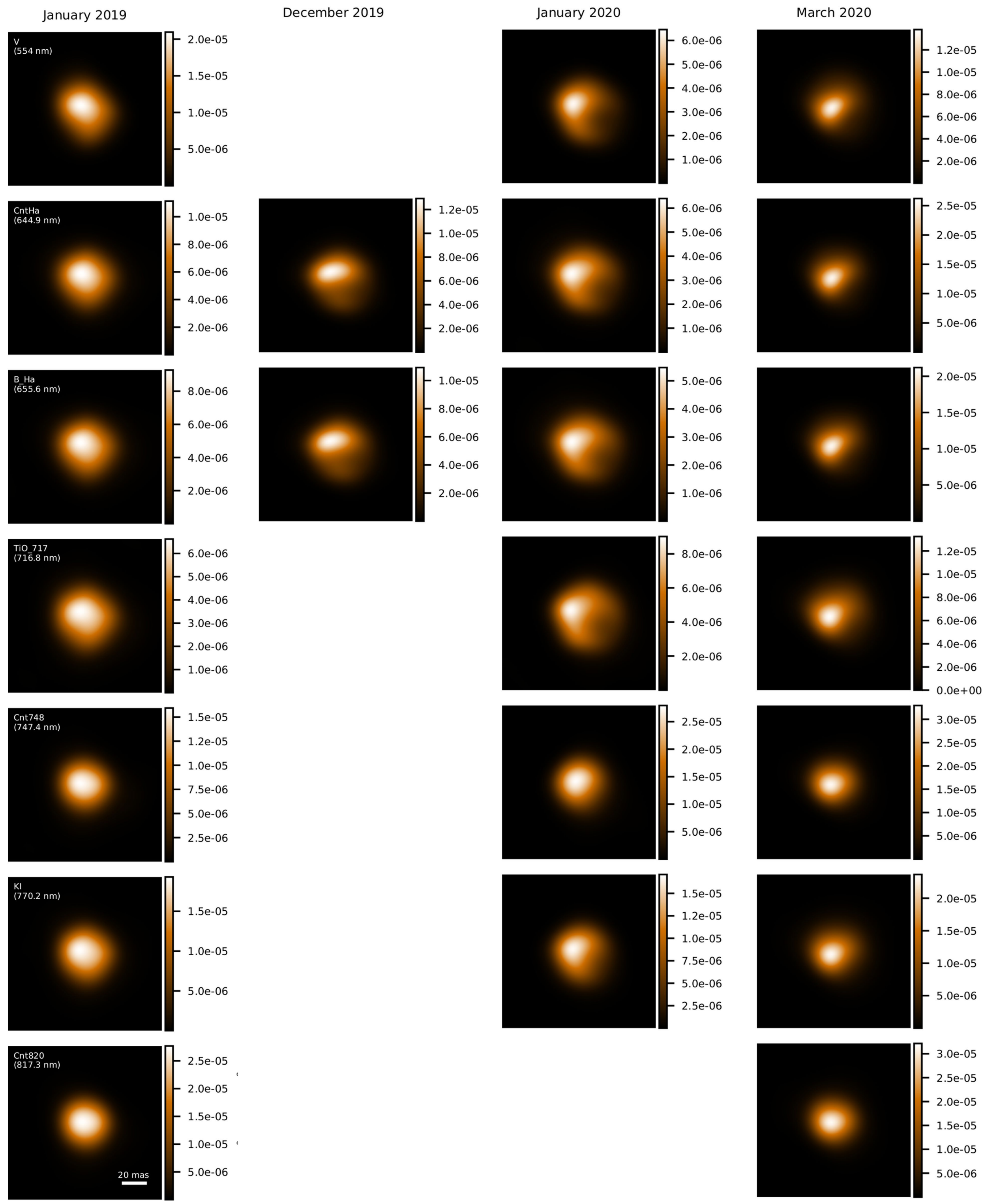

Extended Data Fig. 3 | Deconvolved intensity images of Betelgeuse for the various filters observed with ZIMPOL. The spatial scale is indicated in the bottom left image. North is up; east is left. Each row corresponds to a single filter. Each column corresponds to a single epoch. The colour scales are linear.

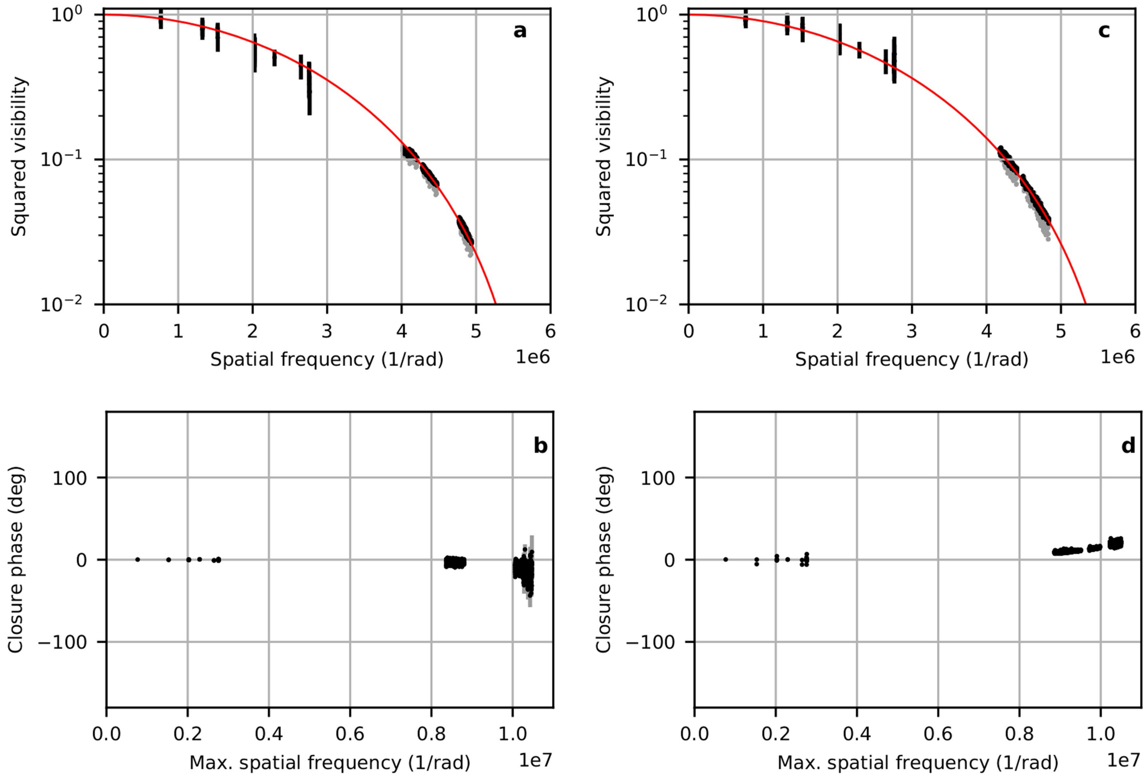

Extended Data Fig. 4 | Fit of the GRAVITY and IRDIS continuum data by a uniform-disk model. The black points correspond to the data and the solid red curve to the model. The grey points correspond to excluded photospheric lines. The error bars correspond to 1 s.d. **a**, Squared visibilities for January 2019. **b**, Corresponding closure phases. **c**, Squared visibilities for February 2020. **d**, Corresponding closure phases.

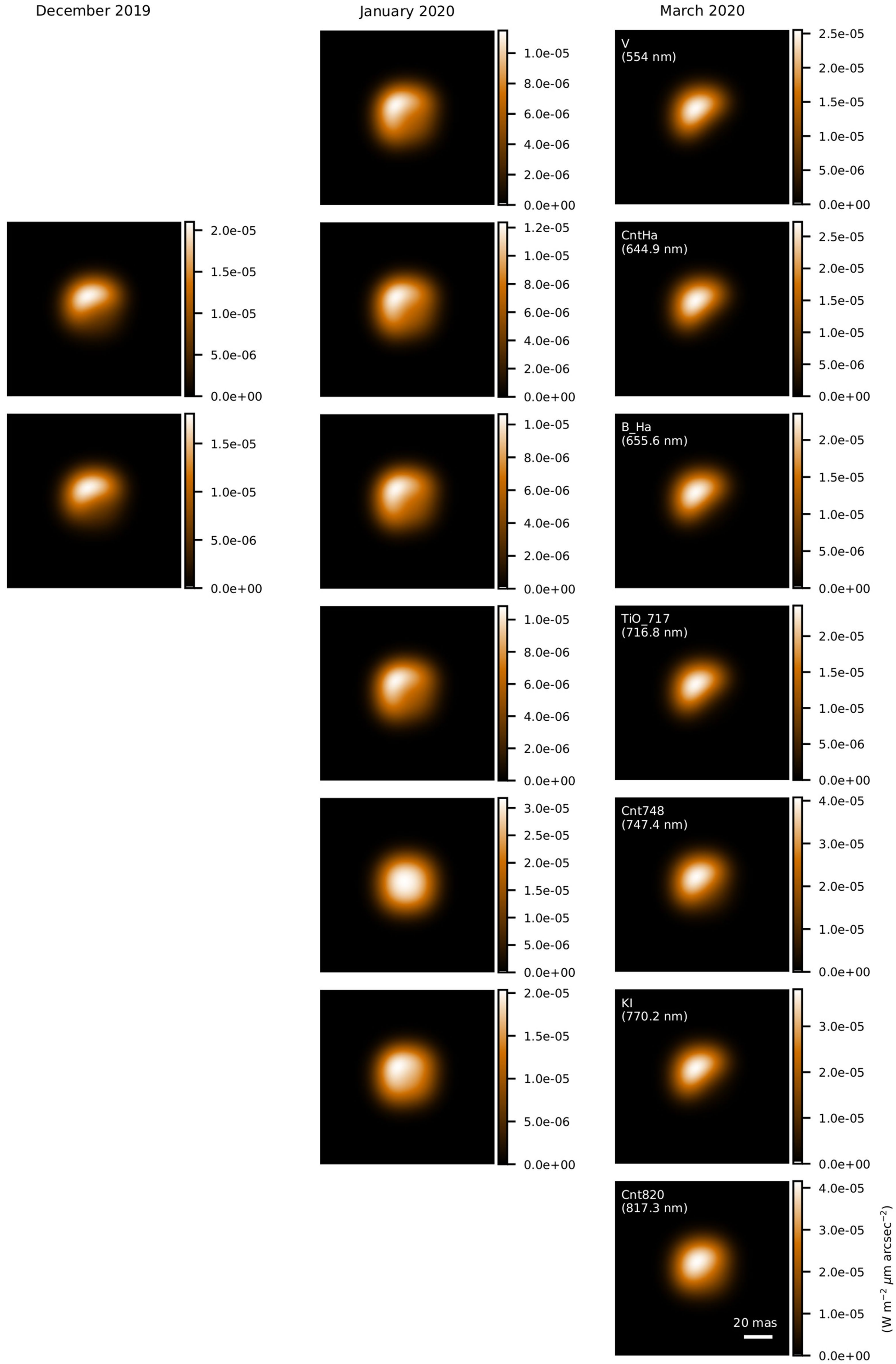

Extended Data Fig. 5 | Best-matching composite PHOENIX model. The spatial scale is indicated in the bottom right image. North is up; east is left. Each row corresponds to a single filter. Each column corresponds to a single epoch. The colour scales are linear.

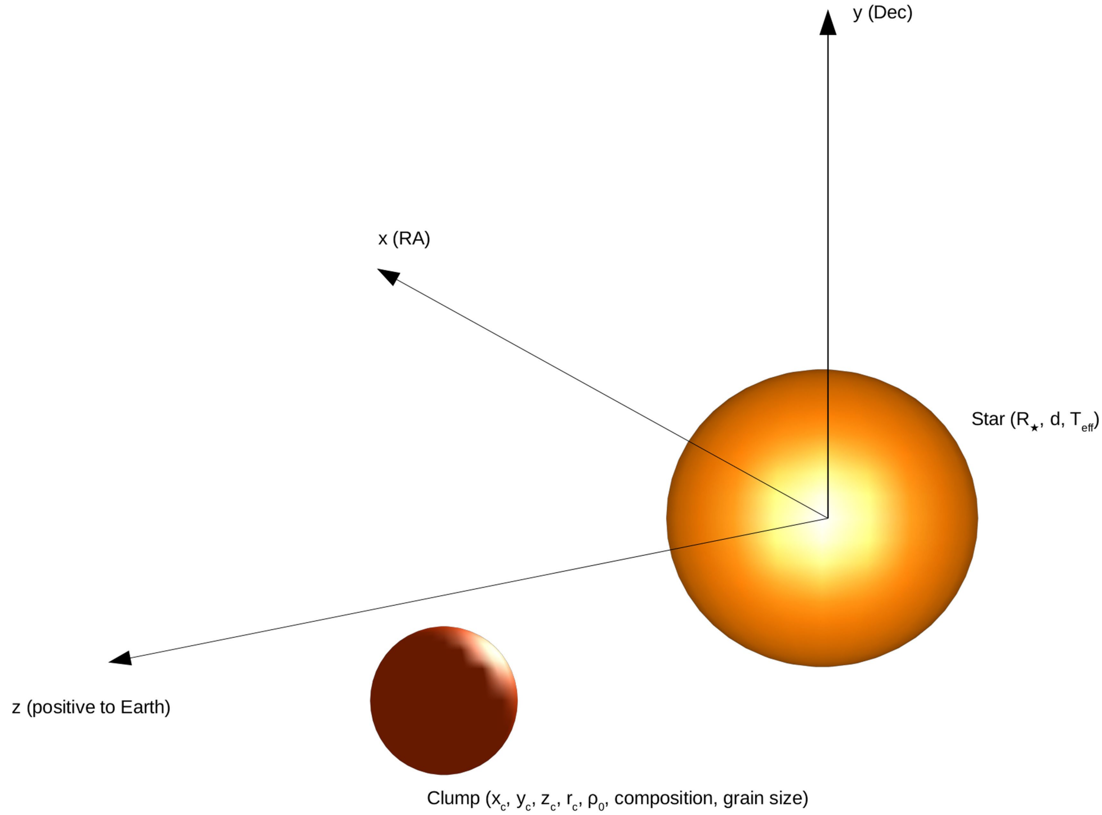

Extended Data Fig. 6 | Identification of the RADMC3D model. Dec, declination; RA, right ascension; R_*, stellar radius; *d*, distance of the star to Earth. The clump parameters are defined in Methods.

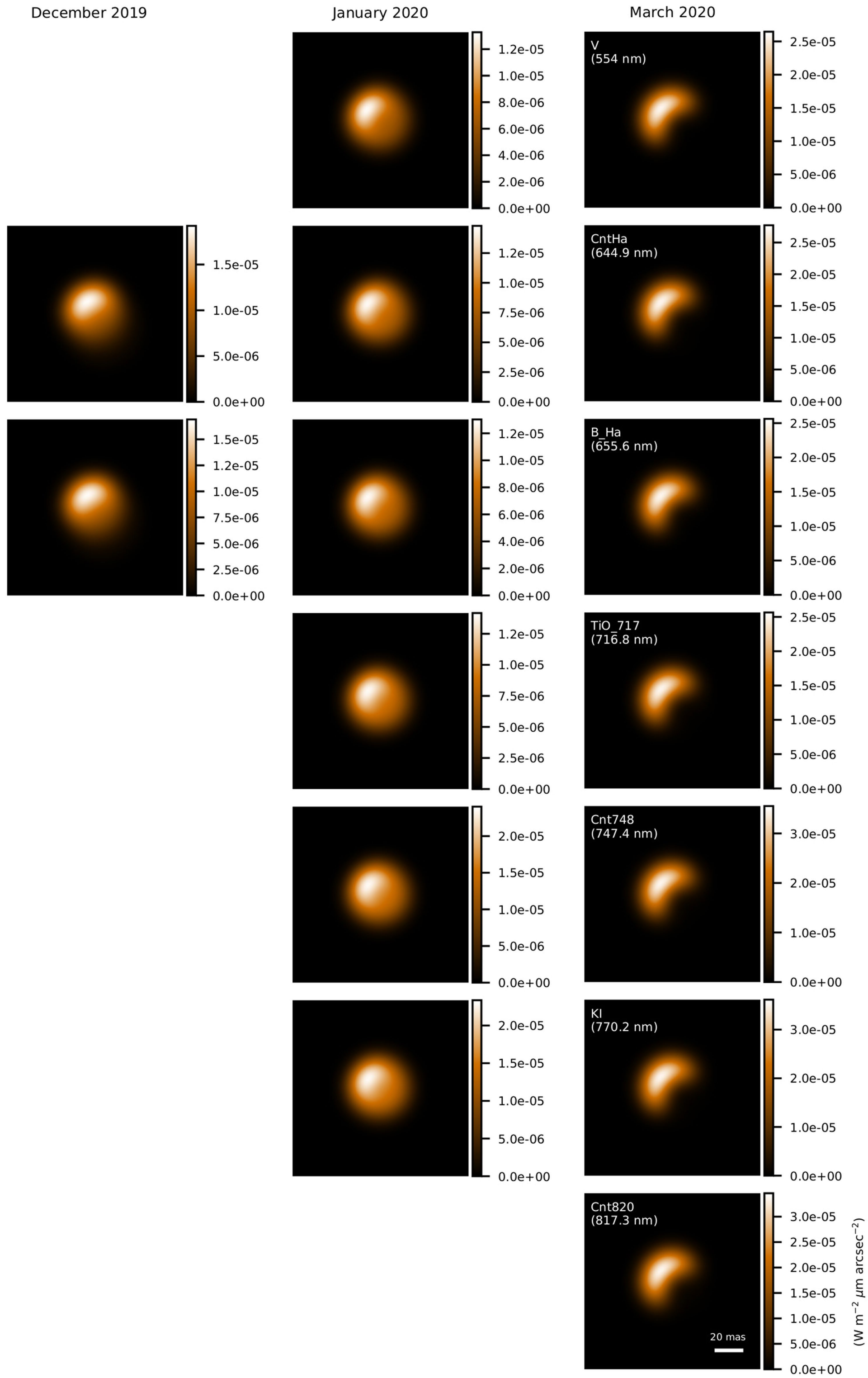

Extended Data Fig. 7 | Best-matching RADMC3D dusty-clump models. The spatial scale is indicated in the bottom right image. North is up; east is left. Each row corresponds to a single filter. Each column corresponds to a single epoch. The colour scales are linear.

Extended Data Table 1 | Log of the VLT/SPHERE observations

VLT/SPHERE-ZIMPOL log									
Date	Time (UT)	Target	Filter 1	Filter 2	ND	DIT (s)	NDIT	Airmass	Seeing (″)
2019-01-01	01:58	Betelgeuse	Cnt_Hα	B_Hα	ND_1	2	6	1.367	0.67
	02:26	Rigel	Cnt_Hα	B_Hα	ND_1	1	10	1.065	0.56
	04:00	Betelgeuse	V	V	ND_2	1.1	6	1.179	0.54
	04:14	Rigel	V	V	ND_2	1.1	6	1.076	0.5
	04:30	Betelgeuse	KI	Cnt_820	ND_2	3	6	1.194	0.77
	04:48	Betelgeuse	TiO_717	Cnt_748	ND_2	6	6	1.213	0.72
	05:25	Rigel	KI	Cnt_820	ND_2	6	6	1.233	0.67
	05:39	Rigel	TiO_717	Cnt_748	ND_2	3	6	1.274	0.54
2019-12-27	03:27	Betelgeuse	B_Hα	Cnt_Hα	ND_1	1	50	1.208	0.52
	03:46	Rigel	B_Hα	Cnt_Hα	ND_2	1	20	1.044	0.43
2020-01-28	02:00	Betelgeuse	B_Hα	Cnt_Hα	ND_1	5	20	1.18	0.83
	02:15	Betelgeuse	V	V	ND_2	5	20	1.179	0.84
	02:45	Rigel	B_Hα	Cnt_Hα	ND_2	4	16	1.098	0.55
	03:04	Rigel	V	V	ND_4	4	16	1.132	0.64
	03:21	Betelgeuse	KI	Cnt_Hα	ND_2	5	8	1.241	0.69
	03:33	Betelgeuse	TiO_717	Cnt_748	ND_4	4	8	1.266	0.69
	03:45	Rigel	KI	Cnt_820	ND_2	6	8	1.242	0.59
	03:57	Rigel	TiO_717	Cnt_748	ND_2	3	8	1.283	0.58
2020-03-18	23:49	Betelgeuse	KI	Cnt_820	ND_2	2	20	1.223	0.74
	23:39	Betelgeuse	TiO_717	Cnt_748	ND_2	2	16	1.239	0.86
2020-03-19	00:16	Rigel	KI	Cnt_820	ND_2	4	12	1.213	0.78
	00:26	Rigel	TiO_717	Cnt_748	ND_2	2	12	1.248	0.62
2020-03-21	00:10	Rigel	B_Hα	Cnt_Hα	ND_2	4	14	1.218	0.75
	00:27	Rigel	V	V	ND_4	20	6	1.28	0.73
	00:53	Betelgeuse	B_Hα	Cnt_Hα	ND_2	5	18	1.42	0.38
	01:11	Betelgeuse	V	V	ND_2	4	22	1.509	0.43

VLT/SPHERE-IRDIS log								
Date	Time (UT)	Target	Filter	ND	NDIT	DIT	Airmass	Seeing (″)
2019-01-01	00:39	ϕ02 Ori	NB_CntK2	NO	100	4.0	1.745	0.76
	00:49	ϕ02 Ori	NB_CO	NO	100	4.0	1.670	0.71
	01:15	Betelgeuse	NB_CntK2	ND_3.5	20	4.0	1.575	0.53
	01:17	Betelgeuse	NB_CO	ND_3.5	20	4.0	1.557	0.55
	01:33	56 Ori	NB_CntK2	NO	20	0.837	1.365	0.68
	01:35	56 Ori	NB_CO	NO	20	0.837	1.358	0.68
2019-12-27	04:35	56 Ori	NB_CO	NO	100	0.837	1.122	0.39
	04:39	56 Ori	NB_CntK2	NO	100	0.837	1.124	0.34
	04:05	Betelgeuse	NB_CO	ND_3.5	100	3.0	1.181	0.33
	04:13	Betelgeuse	NB_CntK2	ND_3.5	100	3.0	1.179	0.38

ND, neutral density; DIT, detector integration time; NDIT, number of acquisitions. The airmass and seeing are provided by the observatory at the start of the acquisition. The filter and neutral density characteristics are available at https://www.eso.org/sci/facilities/paranal/instruments/sphere/inst/filters.html.

Extended Data Table 2 | Log of the VLTI/GRAVITY observations on the A0–B2–D0–C1 quadruplet

Date	Time (UT)	Target	Airmass	Seeing (")
2019-01-29	00:31	56 Ori	1.214	0.74
	00:56	Betelgeuse	1.239	0.68
	01:24	HD 44945	1.194	0.95
	01:47	Betelgeuse	1.183	1.06
	02:14	56 Ori	1.118	0.98
	03:14	56 Ori	1.175	0.97
	03:36	Betelgeuse	1.286	0.94
2020-02-14	00:27	Betelgeuse	1.195	0.66
	00:58	HD 44945	1.150	0.55
	01:49	Betelgeuse	1.185	0.46
	02:28	56 Ori	1.204	0.58

All observations were executed in high-spectral-resolution and dual-polarization mode. The airmass and seeing are provided by the observatory at the start of the acquisition.

Extended Data Table 3 | Modelling results

PHOENIX composite patch			
Parameter	December 2019	January 2020	March 2020
x_{center} (mas)	-7.1	-2.4	-28.4
y_{center} (mas)	-14.2	-2.4	-35.6
radius (mas)	23.7	19.0	45.0
T_{hot} (K)	3,700	3,700	3,700
T_{cool} (K)	3,400	3,400	3,200
$\log \mathcal{L}$	-8.8×10^{6}	-5.5×10^{7}	-4.0×10^{7}
RADMC3D dusty clump			
Parameter	December 2019	January 2020	March 2020
x_c (au)	-1.9	-0.8	-1.9
y_c (au)	-3.0	-0.6	-1.8
z_c (au)	12.5	20.0	20.0
r_c^{in} (au)	6.5	5.0	4.5
ρ_0^{in} (g cm^{-3})	3.2×10^{-19}	4.0×10^{-19}	2.0×10^{-18}

Best-matched parameters for the composite PHOENIX and dust-clump RADMC3D models. For the PHOENIX models, only the fraction of the cool patch recovering the stellar disk is kept in the solution. Pixels outside the stellar disk are set to 0 before convolution with the ZIMPOL point spread function.